Ocean Engineering 363 (2026) 126658

Contents lists available at ScienceDirect

Ocean Engineering

journal homepage: www.elsevier.com/locate/oceaneng

Research paper

Influence of wall proximity on the hydrodynamic response of a wave energy converter

Burhan Yildiz [a,b,*], Davide Dapelo [a], Musa Bashir [a], Nick J. Baker [c], Rose Norman [c], Kayvan Pazouki [c]

[a] Department of Civil and Environmental Engineering, School of Engineering, University of Liverpool, Brownlow Hill, Liverpool, L69 3GH, UK
[b] Civil Engineering Department, Mugla Sitki Kocman University, Mugla, 48010, Turkey
[c] School of Engineering, Newcastle University, Newcastle Upon Tyne, UK

ARTICLE INFO

Keywords:
Wave energy converters
CFD
Marina
RANS
k-ωSST
Marine energy
Renewable energy

ABSTRACT

Marina-installed wave energy converters (WECs) operate under confined hydrodynamic conditions dominated by wave reflection, flow separation, and wall-induced vorticity, which are not adequately captured by traditional low-fidelity approaches such as linear potential flow theory (LPFT). Although computational fluid dynamics (CFD) has been widely applied to offshore WECs, convergence assessment in near-wall marina environments has largely relied on device motions or integral response quantities, with limited attention to turbulence-field accuracy. This study develops a mesh-converged three-dimensional CFD model for wave-structure interaction around a cylindrical WEC positioned near a vertical wall and introduces a novel turbulence-based convergence assessment as a key criterion for resolving wall-induced hydrodynamics. The results demonstrate that near-wall flow structures generate strong velocity gradients and enhanced vorticity, highlighting the importance of including viscous flow dynamics in the modelling framework. The model was applied to over 25 cases to analyse the influence of wall proximity on the hydrodynamic response of a cylindrical WEC. Depending on wall proximity, the kinetic energy of the device can increase by up to a factor of 9.5, demonstrating the critical influence of deployment location on device performance.

1. Introduction

1.1. Background

Wave energy has the potential of surpassing other renewable sources like wind and solar in terms of power intensity, availability and predictability. (Li et al., 2025; Arrosyid et al., 2025). Despite its significant potential, the economic and engineering challenges of wave energy extraction by means of wave energy converters (WECs) prevents investors from capitalizing in this area (Guo and Ringwood, 2021). A key challenge lies in the extreme sea conditions to which these devices are occasionally exposed, often resulting in severe damage or complete loss. An additional barrier is the high capital cost, which generally exceeds that of other renewable energy technologies (Astariz and Iglesias, 2015). A substantial portion of a WEC project's budget is typically allocated to the mooring system and subsea electrical cabling (Satymov et al., 2024).

These challenges can be mitigated by placing WECs within marinas, attached to the existing breakwaters or marina structures. In such sheltered locations, the devices are less exposed to harsh sea conditions, thereby addressing the survivability concerns. Furthermore, electrical cabling cost is minimised, as the location is close to the land.

1.2. System description

This study considers the development of a wave energy converter as part of a marina being developed in South Shields, North East England, Fig. 1. From Baker et al. (2023), the targeted resource in open sea at this location commonly has a period 2-8 s. As the Marina is sheltered and in the mouth of an estuary, the period and amplitude at the location are likely to be smaller. To this end, a low cost, low power heaving concept is being developed in combination with a linear electrical generator (Baker et al., 2025). For efficient co-design of the electrical system, a

* Corresponding author. Department of Civil and Environmental Engineering, School of Engineering, University of Liverpool, Brownlow Hill, Liverpool, L69 3GH, UK.

E-mail addresses: burhan.yildiz@liverpool.ac.uk (B. Yildiz), d.dapelo@liverpool.ac.uk (D. Dapelo), m.b.bashir@liverpool.ac.uk (M. Bashir), nick.baker@newcastle.ac.uk (N.J. Baker), rose.norman@newcastle.ac.uk (R. Norman), kayvan.pazouki@newcastle.ac.uk (K. Pazouki).

https://doi.org/10.1016/j.oceaneng.2026.126658
Received 29 January 2026; Received in revised form 17 June 2026; Accepted 17 June 2026
Available online 21 June 2026

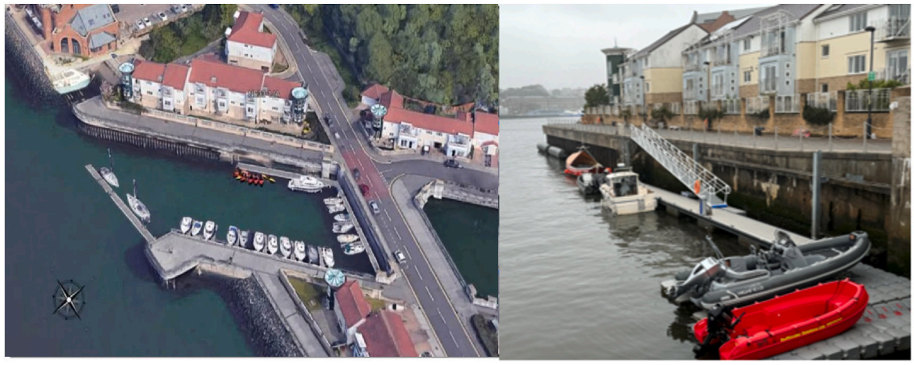

Fig. 1. The marina being developed in South Shields, North East England.

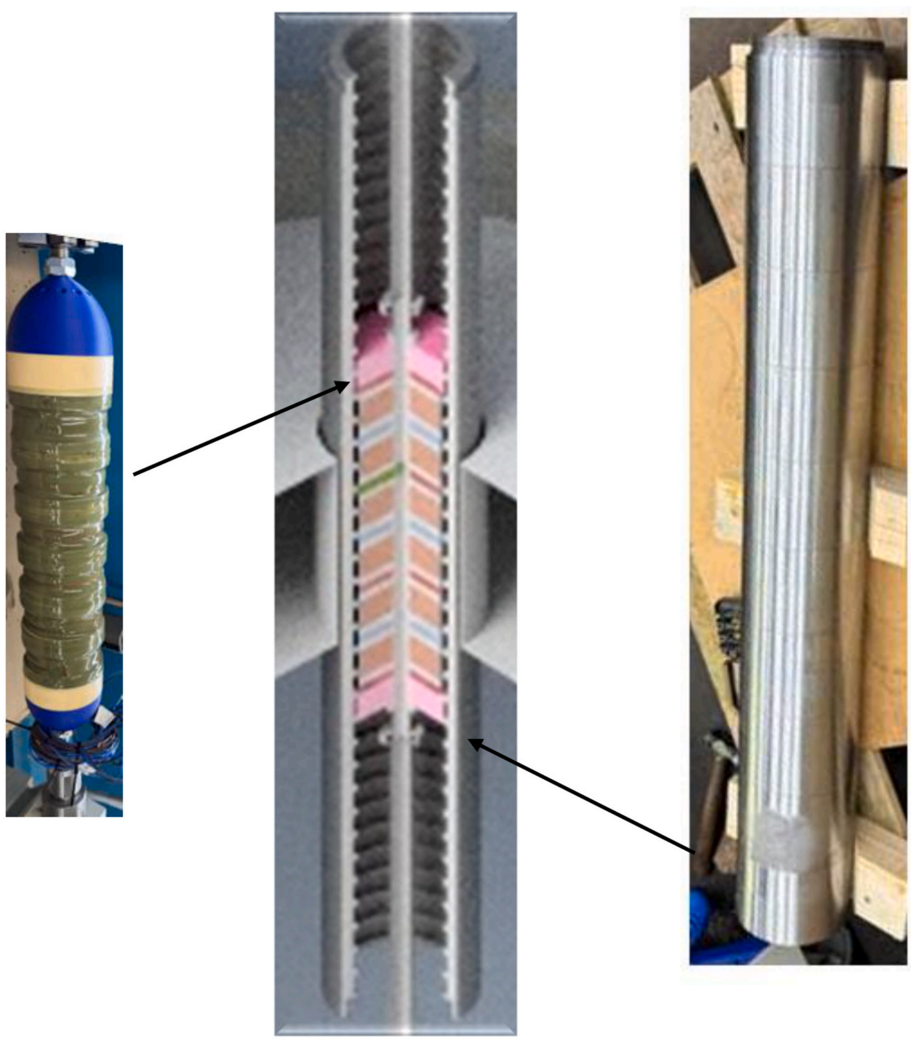

Fig. 2. A linear generator developed for wave energy consisting of an encapsulated stator (left) enclosed in a tubular translator (right).

detailed understanding of the buoy operation is required, and particularly how its predicted yield varies with exact location within the marina. Specifically, deployment position relative to the marina wall is considered in this work.

1.3. Power extraction and power take off in wave energy converters

Typically, in a heaving buoy wave energy converter the wave force acts on a semi submerged body causing it to oscillate. The resulting motion is used to generate electrical power through provision of an opposing force by an electrical machine. The peak velocity of the buoy is at least one order of magnitude slower than that found in other applications. Either a speed enhancing mechanical linkage such as a gearbox is required, or an electrical machine capable of operating at low speed must be developed. This is referred to as ‘direct drive’ power take off.

In order to reduce costs and almost eliminate maintenance requirements, a number of researchers are developing linear generators for use in direct drive WECs. The electrical machine developed for this purpose by the authors is detailed in Farahani et al. (2023) and shown in Fig. 2. In a full scale WEC, the power take off (PTO) force from the generator is used to control the device oscillation. Depending on the selected control strategy, the PTO force may include resistive, reactive, or more advanced control components. In a low power low cost WEC, however, it is more likely the power take off force will be related to velocity, corresponding to a damping-type behaviour. Wave energy control is a complex subject, and there is interdependence between WEC design, PTO design and control strategy (Onslow and Stock, 2025).

In this work, which focuses on resource prediction and hydrodynamic modelling, PTO control is not explicitly considered, and unconstrained oscillation amplitude is instead used as a relative indicator of hydrodynamic response and potential energy capture. The results are therefore primarily applicable to point absorber type WECs operating under similar oscillatory dynamics, independent of the specific PTO implementation or control algorithm.

1.4. Modelling the resource in the marina

Reduced wave height in enclosed marina environments leads to significantly lower power output than open-sea locations (Foteinis, 2022). This raises questions about the feasibility and optimality of deploying WECs in marinas. To assess this, accurate prediction of the system's potential for generating a power output is essential. This involves the prediction of kinetic energy response of the WEC which can be carried out using hydrodynamic models.

Hydrodynamic modelling of flow around WECs has been carried out using simpler to more complex methods considering the aim and the resources. Notable approaches, listed from lowest to highest fidelity, include analytical mathematical models (Yang et al., 2023), boundary element methods (BEM) based on linear potential flow theory (LPFT) (Kara, 2021), higher-order or nonlinear BEM formulations that account for wave nonlinearity and large-amplitude free-surface motion (Ning et al., 2015), high-order spectral methods (Ducrozet et al., 2016), and computational fluid dynamics (CFD) approaches (Windt et al., 2020; Alletto, 2022), which resolve viscous and turbulent effects. LPFT has been widely adopted due to its computational efficiency and ease of implementation, assuming the flow is inviscid and irrotational. However, this assumption breaks down under energetic wave conditions, where viscous drag, flow separation, vortex shedding, and other nonlinear hydrodynamic effects become significant (Windt et al., 2018). In particular, when wave height is large compared to WEC dimensions, or when WECs have sharp edges or geometric features prone to inducing viscous effects, potential flow solvers generally fall short from capturing key dynamic features (Wolgamot and Fitzgerald, 2015; Bharath et al., 2018). Chen et al. (2017) compared the results from a WAMIT-based LPFT model and a CFD model using ANSYS Fluent. The mean relative difference in predicted buoy displacements was only 1% for 1 m wave heights, but it considerably increased—up to 89%—for 3 m wave heights.

Previous studies investigating WECs near coastal or marina structures have reported that wall proximity can significantly alter hydrodynamic coefficients, resonance behaviour, and power absorption characteristics. Kara (2021, 2022) employed LPFT-based approaches to examine wall-induced wave amplification and demonstrated that reflected waves may enhance device response under certain geometric configurations. Wang and Dong (2023) investigated efficiency of a WEC installed at a semicircular opening of a breakwater by using LPFT methods. Kang et al. (2024) investigated hydrodynamic performance of a WEC array placed close to a vertical wall using linear water theory. Li et al. (2024) demonstrated a performance increase in energy absorption of a WEC close to the wall when its location is close to the antinodes of the standing wave field. They used LPFT based methods in their analysis. Ding (2024) extended the analysis using a two-dimensional CFD framework and showed that confinement effects increase local flow asymmetry and vortex formation. More recently, Kang et al. (2025) and Heo et al. (2025) investigated wave reflection and hydrodynamic interaction mechanisms in semi-enclosed environments, although their analyses remained limited by reduced-order or weakly nonlinear formulations.

Despite the growing interest in wall–WEC interaction, relatively few studies have employed three-dimensional CFD models capable of resolving the complex turbulent flow structures generated in confined environments. Yang et al. (2023) investigated the influence of wall proximity on WEC hydrodynamics and optimised a combined WEC–-breakwater configuration using a 3D CFD framework. Song et al. (2024) analysed the oscillatory response of a WEC positioned near a vertical wall. Khatibani et al. (2025) further examined the motion of a WEC adjacent to a floating platform using CFD simulations. However, the convergence and validation strategies adopted in these studies were primarily based on device motion or integral response quantities, with limited consideration of turbulence-field resolution and near-wall flow accuracy.

1.5. Approach

This study addresses the methodological gap of excluding turbulence quantities from convergence analysis by developing a three-dimensional model for wave energy converters deployed in marinas. Unlike previous studies that assess convergence primarily through device motion or power output, the present work explicitly examines turbulence quantities, demonstrating their critical role in accurately resolving near-wall and high-vorticity flow conditions. This approach addresses known limitations of low-fidelity and position-based convergence methods in constrained environments. The results show that the predicted WEC position converges more rapidly than the turbulent fields, which may lead to misleading conclusions when applied to complex flow conditions. Following convergence assessment, the model was validated against an experimental heave-decay benchmark and subsequently employed in a numerical campaign comprising more than 25 cases to investigate the effect of wall proximity on the flow field and WEC motion. The main aims of this paper are therefore: (1) to establish a mesh-converged 3D CFD model for solving flow hydrodynamics around a cylindrical WEC device; (2) to demonstrate the importance of turbulent quantities as part of the mesh convergence assessment methodology; and (3) to apply the model to examine the effect of wall proximity on the kinetic energy response of the WEC.

2. Method

Flow hydrodynamics around a cylindrical WEC was modelled by using a 3D mesh in OpenFOAM v2412 (Weller et al., 1998; OpenCFD Ltd, 2026). Its motion was modelled under uniform wave conditions with a wave height of 0.05 m and a wave period of 3.14 s considering regular wave settings at a marina environment. A 1 m water depth was assigned below the centroid of WEC in the numerical wave tank when the WEC is in a stationary condition. A finite-volume approach was applied by solving the Reynolds Averaged Navier Stokes (RANS) equations. A multiphase flow solver of OpenFOAM, interFoam, which uses the Volume-Of-Fluid approach (VOF - Hirt and Nichols, 1981) was used to track the water-air interface. This method defines a volume fraction parameter, α, for water in each computational cell and calculates representative densities and viscosities. For example, the density at a cell is estimated by using the densities of water, ρ_w and air, ρ_{air} as $\rho = \alpha\rho_w + (1-\alpha)\rho_{air}$. The model equations are given below:

$$\frac{\partial u_i}{\partial x_i} = 0 \tag{1}$$

$$\frac{\partial(\rho u_i)}{\partial t} + \frac{\partial(\rho u_i u_j)}{\partial x_j} = -\frac{\partial p}{\partial x_i} + \frac{\partial}{\partial x_j}\left(\mu\frac{\partial u_i}{\partial x_j} - \rho\overline{u_i' u_j'}\right) + \rho g_i + T\kappa\frac{\partial \alpha}{\partial x_i} \tag{2}$$

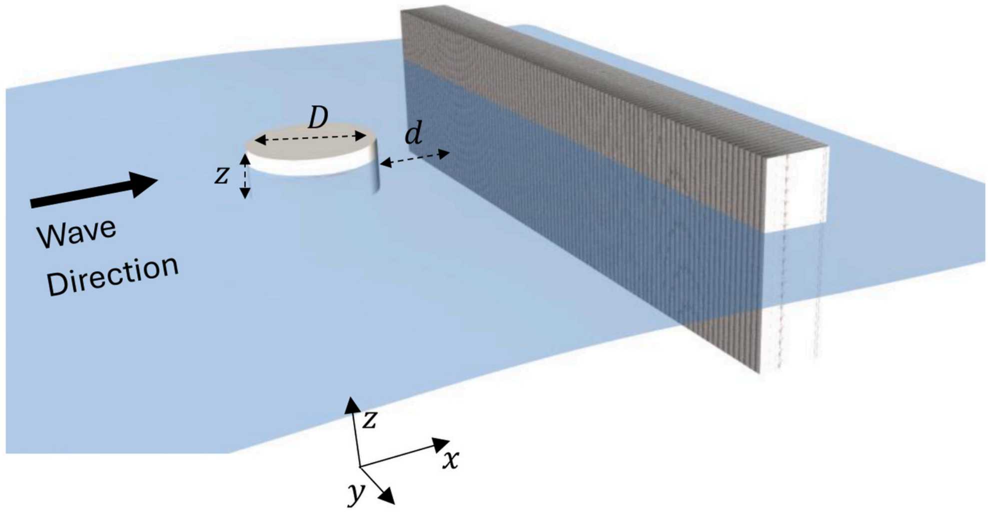

Fig. 3. A schematic representation of a cylindrical WEC beside a vertical wall.

where u_i is the time-averaged velocity in direction x_i, p is the pressure, μ is the molecular viscosity and $\rho\overline{u_i'u_j'}$ is the Reynolds stress term. The last term of Equation (2) on the right adds the effect of surface tension with T denoting the surface tension with a magnitude 0.07 N/m for air-water interfaces. The interface curvature is denoted by κ. An additional advection equation is written for the conservation of α as given below:

$$\frac{\partial \alpha}{\partial t}+\frac{\partial(\alpha u_i)}{\partial x_i}+\frac{\partial}{\partial x_i}\left(\alpha(1-\alpha)u_i^r\right)=0 \tag{3}$$

where u_i^r denotes the artificial interface-compression velocity introduced in the MULES (Multidimensional Universal Limiter with Explicit Solution) algorithm to counteract numerical diffusion and preserve interface sharpness near the phase boundary (Rusche, 2002; OpenCFD Ltd, 2026). The compression velocity is active only in cells containing the interface and vanishes in pure-phase regions.

The Reynolds stress term in Equation (2) was modelled by using the Boussinesq approximation. The stress term was modelled by introducing a turbulent viscosity term μ_t. The turbulence model used in this study is k-ω SST model where k is turbulence kinetic energy and ω is the specific turbulence dissipation rate defined as $\omega = {}^{k}\!/_{\varepsilon}$ where ε is turbulence dissipation rate. The k-ω SST model was proposed as a blended model that employs the k-ω model (Wilcox, 2008) near wall regions and the k-ε model (Launder and Spalding, 1974) in the regions away from the wall (Menter, 1994). The k-ε model defines μ_t as $\mu_t = \rho C_\mu \frac{k^2}{\varepsilon}$ where C_μ is a model constant and was taken as 0.9 in this study. It solves for two additional transport equations written for k and ε. k-ω model defines μ_t as $\mu_t = \frac{k}{\omega}$ and includes transport equations written for k and ω. The k-ω SST turbulence model was employed due to its improved performance in adverse pressure gradient and flow separation regions compared to standard two-equation eddy-viscosity models, particularly the k-ε model, as demonstrated in benchmark studies (Menter, 1994; Menter et al., 2003). Previous studies have also demonstrated good agreement between numerical predictions and experimental data when applying the k-ω SST turbulence model to separated flows in environmental fluid dynamics (Jiang et al., 2018; Yildiz and Uijttewaal, 2025).

The dimensions of the computational domain were selected based on safe distances for wave development and absorption, with approximately one wavelength from the WEC to the inlet and about two and a half wavelengths to the outlet, consistent with the recommendations of (Jacobsen et al., 2012). One half of the domain was simulated using the symmetry condition in the lateral direction. The side boundary was positioned more than one wavelength away from the WEC centroid and assigned a symmetry boundary condition to minimize its influence on the WEC motion. Stokes second-order wave generation was applied at the inlet being consistent with the wave settings (Le Méhauté, 2013). Active wave absorption, as implemented in OpenFOAM, was used at the outlet. A schematic view of the domain in perspective view and in side view are given in Figs. 3 and 4, respectively.

The mesh was developed by considering a base mesh without the WEC or a marina wall. In this mesh, the region around the free surface was refined and gradual refinements in the horizontal directions were applied aiming at a refined mesh with almost cubic elements at the region around the WEC. When the WEC was implemented, additional refinement was applied at the WEC perimeter and layers were added next to the perimeter to capture the boundary layer around it. A mesh convergence study was applied considering six meshes developed using the same strategy and applying varying refinements at the base mesh. The mesh used in the study includes slightly more than 7 million cells in the domain by assuring the dimensionless wall distance (y^+) values less

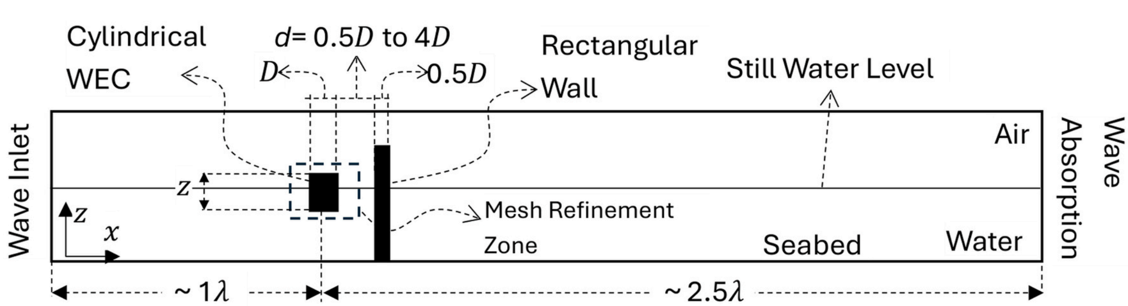

Fig. 4. Side view of the domain (not to scale) (λ: wavelength, D: Diameter of the cylindrical WEC, z: height of the WEC).

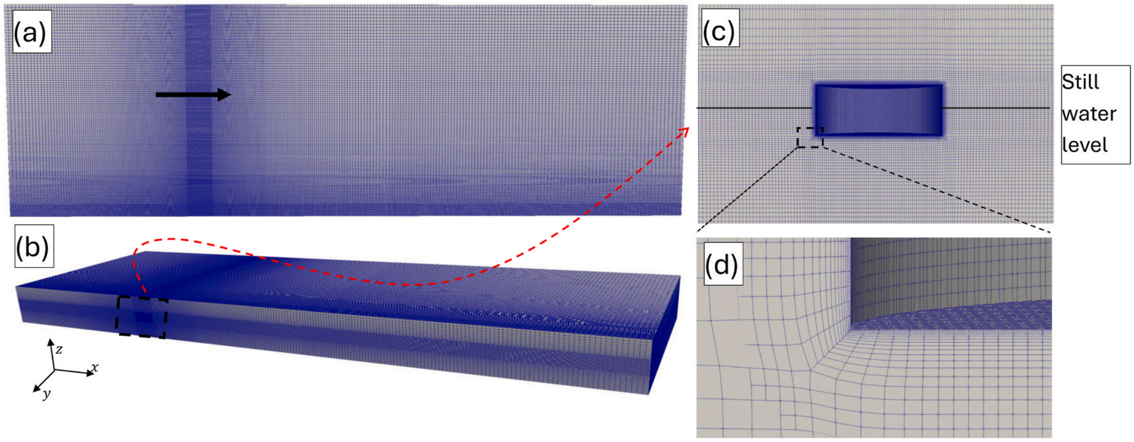

Fig. 5. Computational mesh (M4) used for simulations involving the WEC without the marina wall: (a) Top view with wave direction indicated (b) Perspective view (c) Side view highlighting the mesh around the WEC; (d) Close-up view of the added layers around the WEC.

Table 1
Mesh data for the alternatives (the number of processors used parallel at each run is given in parentheses).

Mesh	Total Cell Count	Max y^+ around the WEC	Total run time (hrs.)
M0	371,374	9.1	0.8 (20 proc.)
M1	1,062,282	7.3	5.4 (80 proc.)
M2	2,300,400	6.4	25.5 (80 proc.)
M3	4,234,255	5.9	9.6 (160 proc.)
M4	7,018,225	5	19.34 (160 proc.)
M5	10,681,463	4.8	45.54 (160 proc.)

than 5 at almost every portion of the WEC boundary at each time step. Views of this mesh are given in Fig. 5.

The discretization schemes were selected as at least second order for convective terms considering the accuracy. The simulations were run at least for 70 s, and almost uniform oscillations were observed at the WEC after 40 s. The time step in the simulations was used as modifiable considering Courant number less than 1 at each time step.

To qualitatively investigate the effect of wall proximity on the wave height observed by the WEC, three cases were developed by using the same meshing strategy applied at the converged mesh alternative (M4) using varying wave periods. In these cases, a vertical wall with a width of 10 m and a height of 1.5 m was placed at 0.5 m, 1.0 m, 1.5 m, 2 m, 2.5 m, 3 m, 3.5 m and 4 m away from the WEC and tested separately in each case. The region occupied by the wall was simply removed from the mesh and simple refinements were applied around it. The tests were repeated for wave periods of $\pi/2$ and $3\pi/2$ s to observe the effect on the WEC motion.

3. Results and discussion

3.1. Model verification

Verification of the model was ensured through a mesh convergence study for the case with a WEC and without a wall. For the tested mesh alternatives, total cell count and total run time (based on parallel computation using a varying number of processors) are given in Table 1. Due to the unsteady nature of the flow around the oscillating WEC, velocities, and consequently y^+ values, change over time. As also noted by Windt et al. (2020), it was not straight forward to define a single y^+ value valid across all time steps. In this study, the wetted perimeter of the WEC was rendered from the simulation results and the y^+ values were plotted at the last three recorded time steps as $t = 40$, 45 and 50 s. The maximum values of the observed ones are recorded in Table 1. While ideally this check should have been performed at every time step, it was conducted at 5-s intervals due to practical limitations.

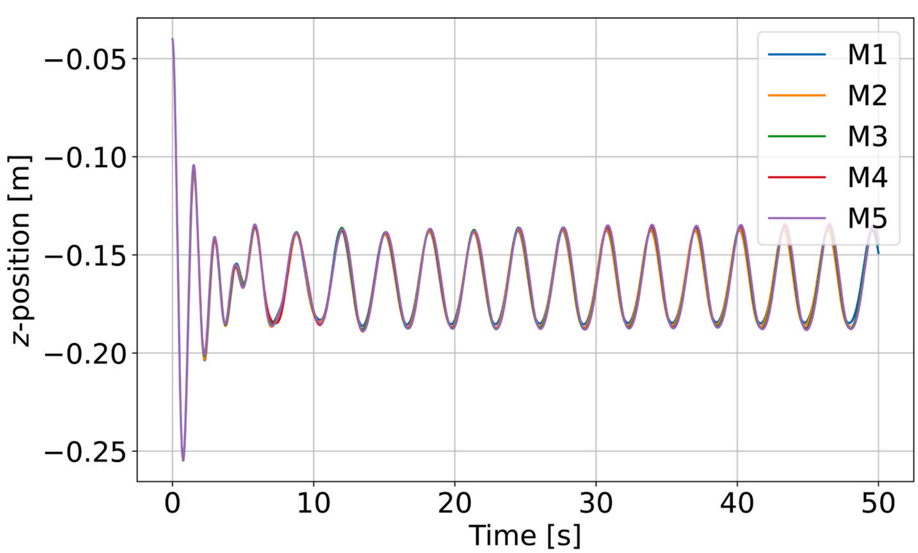

Fig. 6. Comparison of simulated time series of z-position of centre of mass of WEC at varying mesh alternatives.

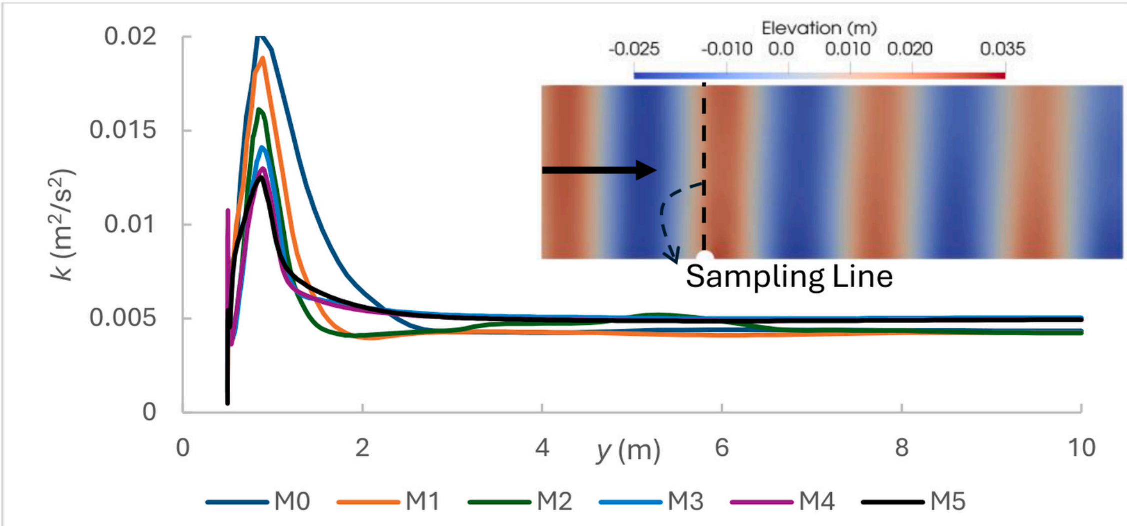

Fig. 7. Comparison of simulated turbulent kinetic energy (k) distributions of each mesh alternative at $t = 50$ s over the line indicated in the embedded image. The embedded image shows the simulated water surface at $t = 50$ s for M4 with elevations and wave direction indicated.

The results were compared by considering the position of the WEC's centre of mass, and turbulent kinetic energy (k) values. Fig. 6 shows the time series of the position of the WEC's centre of mass for all the alternatives tested. The results show that the oscillations of the WEC become almost uniform after 15 s of the simulations. The results of the alternatives do not differ significantly when the mesh was finest. In particular, the difference of the wave heights from simulations M3 and M4 were less than 0.5%. This is an indication of clear convergence if only this parameter is to be considered in the tests.

Furthermore, the turbulence quantities were monitored at the simulated water surfaces. A straight line extending in the lateral direction passing through the centre of the WEC was considered and the distribution of k over it was plotted for each alternative as given in Fig. 7. Unlike the early convergence observed from the WEC's z-position time series, the results show a monotonic convergence only starting from run M3, and then to up to M5. Between runs M4 and M5, the variances were small at every compared point, being below 3%. It was therefore concluded that convergence was achieved. As such, run M4 was considered as the best balance between accuracy and numerical expense, and was selected for further analysis on the cases considering the effect of wall proximity on the hydrodynamic response of the WEC. A comparison between the results reported in Fig. 6 and the ones presented in Fig. 7 shows that the convergence of WEC position does not necessarily imply convergence of the turbulent quantities. This distinction becomes particularly important in confined environments where flow separation, vorticity generation, and wall-induced shear layers play a significant role in local hydrodynamics.

3.2. Model validation

For the experimental validation of the model, a heave-decay test case reported by Kramer et al. (2021) was used. Although the test conditions do not exactly match those of the primary case considered in this study, this dataset was selected due to the absence of experimental measurements for heave-only motion under conditions representative of the present work. Future works will fill this experimental gap. Nevertheless, the heave-decay experiment captures the key mechanisms governing the coupling between multiphase free-surface oscillations and the motion of

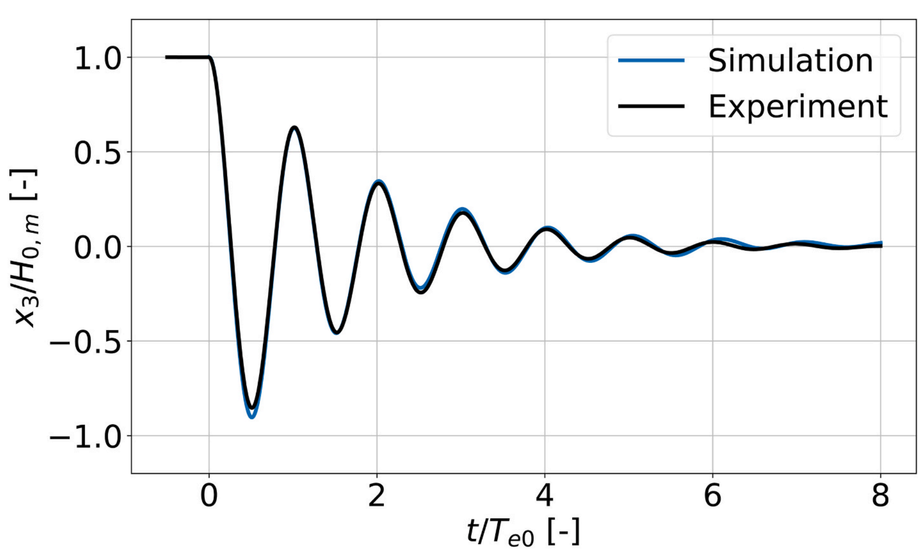

Fig. 8. Comparison of the experimental (Kramer et al., 2021) and numerical results in terms of normalized vertical position of the sphere as a function of normalized time.

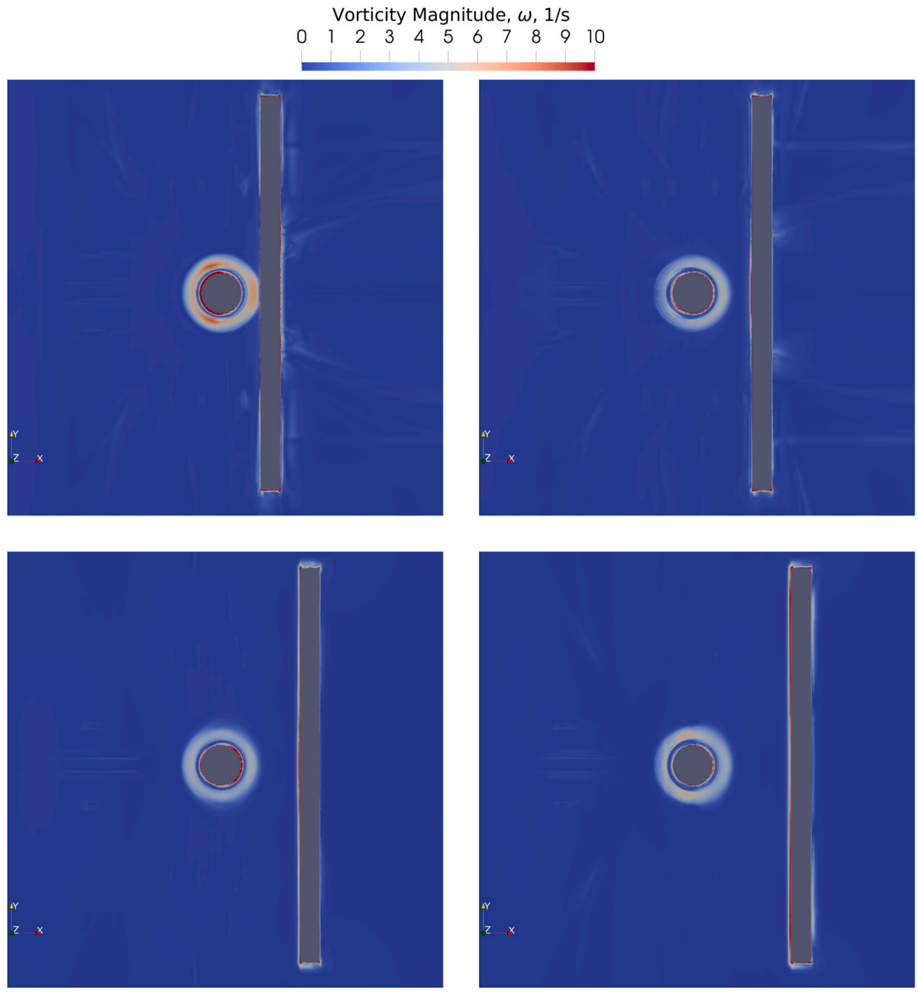

Fig. 9. Variation of vorticity magnitude (ω) on the simulated water surface for varying distances between WEC and the wall. Panels are ordered row-wise (top left, top right, bottom left, bottom right), with separation distances (d) of 0.5, 1.0, 1.5, and 2.0 m, respectively.

an immersed object. It therefore provides a relevant benchmark for assessing the model's ability to reproduce the dominant fluid–structure interaction behaviour. In the experiments presented by Kramer et al. (2021), a 30-cm-diameter sphere was released from a 3-cm-height above still water, and the temporal evolution of the location of its centre-of-mass was recorded.

The case was modelled using the same approach described in Section 2, with a computational mesh constructed to achieve y^+ values comparable to those of the M4 mesh defined in that section. In the experiments, the vertical position of the sphere was recorded as a function of time. Both the vertical coordinate and time were nondimensionalized as $x_3/H_{0,m}$ and t/T_{e0}, where x_3 is the vertical coordinate, $H_{0,m}$ is the release height, t is time, and T_{e0} is the characteristic time scale.

Fig. 8 demonstrates that the simulation closely reproduced the experimental measurements, with only minor deviations. Considering that the total height covered by the sphere was very small which required very high accuracy, these small discrepancies could be tolerated, and the model was considered as validated.

3.3. *Effect of wall proximity on flow dynamics*

As stated previously, to observe the effect of wall proximity on the flow dynamics and kinetic energy response, simulations including a vertical wall behind the WEC were developed and executed for 70 s after which the oscillations appeared to be uniform. The simulated water surfaces for each case were estimated, and the variations of vorticity magnitude, ω, over the water surface were plotted at $t = 70$ s at each tested d value (Figs. 9 and 10). The figures clearly indicate an increase in vorticity magnitude around the WEC when the wall gets closer to it, having the highest surrounding vorticity magnitudes for $d = 0.5$ m and lowest for $d = 4$ m.

When the WEC approaches the vertical wall, the reflected wave field increasingly interacts with the incident waves, modifying the local hydrodynamic environment around the device. Fig. 11 compares the free-surface velocity vectors for the two extreme cases of $d = 0.5$ m and $d = 4$ m. This figure shows substantially larger velocity magnitudes around the WEC for $d = 0.5$ m. Due to the no-slip and stagnation effects imposed by the solid boundaries, the accelerated flow within the narrow gap produces significantly larger velocity gradients and shear stresses near the WEC surface. These enhanced shear layers contribute directly to the increased vorticity generation observed in the confined cases. The intensified viscous and shear stress effects act as a dissipative mechanism that opposes the oscillatory motion of the WEC, leading to increased hydrodynamic damping and reduced body response. Accurate resolution of these stress-dominated regions is therefore essential for correctly capturing the destructive influence of viscosity on WEC oscillations and for reliably predicting the performance of confined wave energy systems. This highlights the importance of employing a sufficiently high-fidelity numerical model for resolving the near-body flow physics.

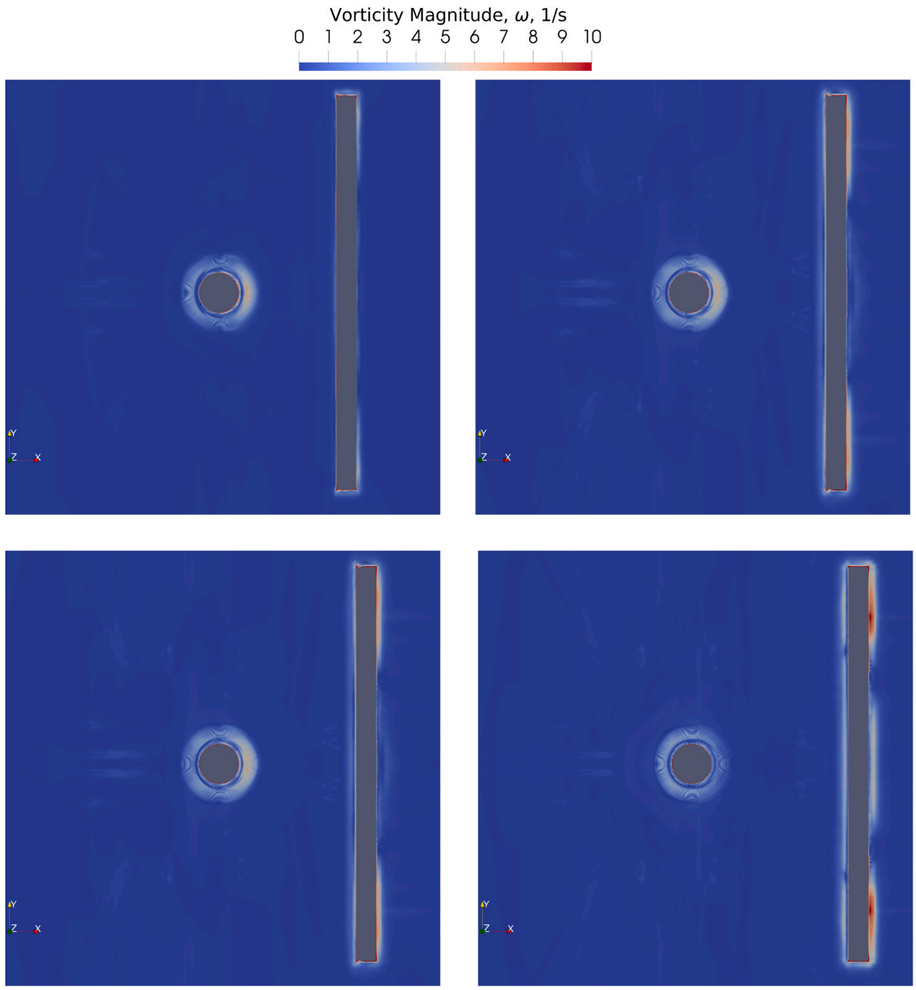

Fig. 10. Variation of vorticity magnitude (ω) on the simulated water surface for varying distances between WEC and the wall. Panels are ordered row-wise (top left, top right, bottom left, bottom right), with separation distances (d) of 2.5, 3.0, 3.5, and 4.0 m, respectively.

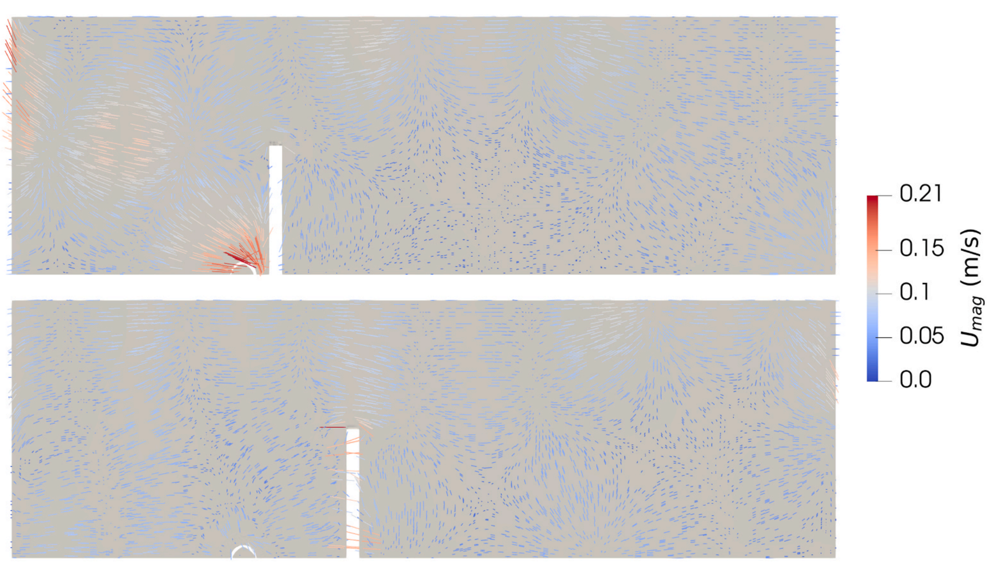

Fig. 11. Velocity vectors on the free surfaces at the final time step for the W1 cases: (top) $d = 0.5$ m; (bottom) $d = 4.0$ m. Vectors are scaled and coloured according to velocity magnitude.

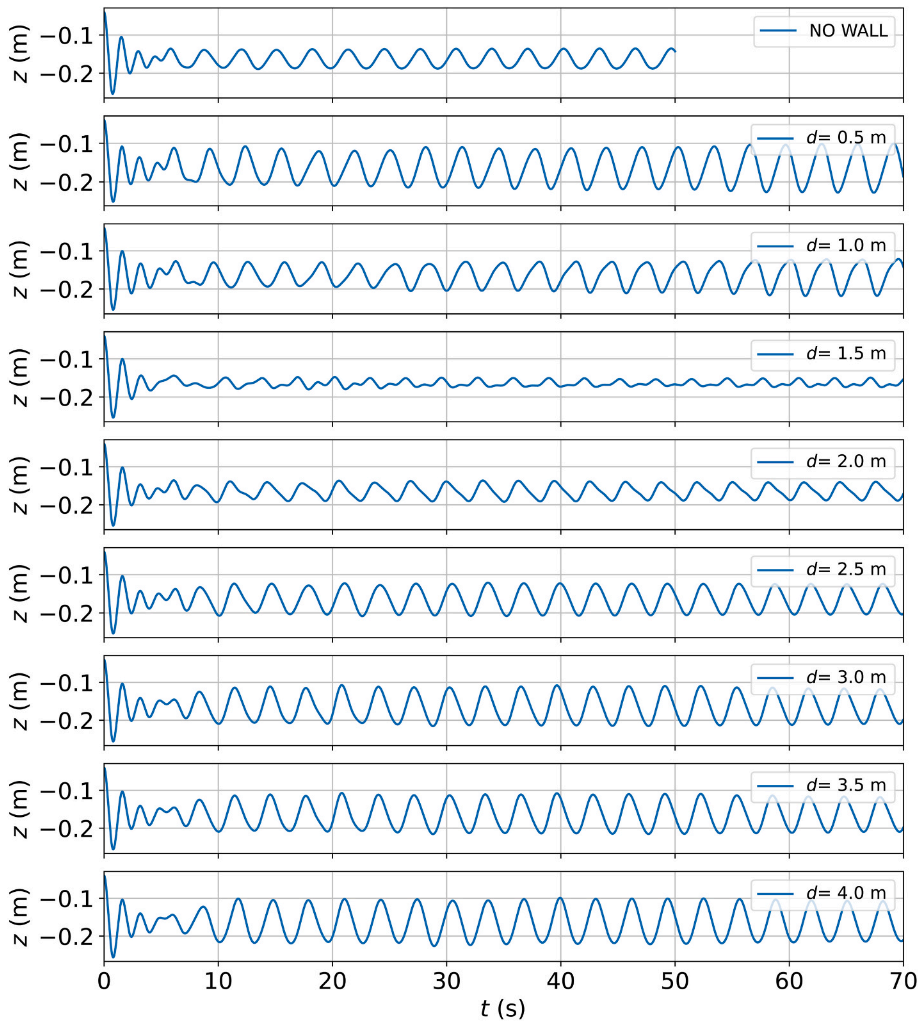

Fig. 12. Time series of the z-position of the centre of mass of the WEC at varying distances from the wall, d for the first wave setting ($T = 3.14$ s). The output of the case without a wall is also given at the top panel for comparison.

3.4. Effect of wall proximity on WEC oscillations

The vertical displacement of the WEC's centre of mass over time for d varying from 0.5 to 4 m with steps of 0.5 m, is shown in Fig. 12, together with the no-wall case. In all cases, a quasi-oscillatory trend is observed. A vertical displacement of approximately twice that of the no-wall case occurs at $d = 0.5$ m. Increasing d results in a decrease of the displacement up to the minimal value observed at $d = 1.5$ m. Further away from that distance, the displacement of the WEC starts to increase again. Finally, at $d = 4$ m, the displacement becomes greater than that observed at $d = 0.5$ m.

To assess the influence of wave period, simulations were repeated using two more wave settings with a wave period of $T = 1.57$ s (half the period of the first wave settings, wave setting: W2) and a wave period of $T = 4.71$ s (1.5 times the period of the first wave settings, wave setting: W3). The corresponding time histories of the WEC motion are presented in Figs. 13 and 14. Compared with Fig. 12, the relationship between oscillation amplitude and d changes significantly for these wave conditions. For $T = 1.57$ s, the minimum response occurs at $d = 2$ m, while for $T = 4.71$ s the oscillation amplitude generally decreases with increasing d, reaching its minimum at $d = 4$ m. The largest oscillations are observed at the closest wall condition ($d = 0.5$ m) for $T = 4.71$ s. In addition, for W2 case, the response at $d = 1$ m exceeds that at $d = 0.5$ m, indicating a non-monotonic dependence on wall distance.

For a more quantitative comparison, the time-averaged kinetic energy of the WEC was evaluated using the instantaneous velocity extracted from the simulations as follows:

$$K = \frac{1}{t_1 - t_0} \int_{t_0}^{t_1} \frac{mV^2}{2} dt \tag{4}$$

where the averaging interval t_1 - $t_0 = 10$ s corresponds to the last 10 s of the simulations, during which the oscillations have reached statistically steady state. Here, m is the mass of the WEC, V is the simulated instantaneous velocity of the WEC and dt is the time step used in the simulations.

The kinetic energy was normalized with respect to the no-wall case as $K^* = K_i/K_r$, where K_i is the time-averaged kinetic energy of the WEC corresponding to a given wall distance d, and K_r is the time-averaged kinetic energy of the reference case without a wall. Both quantities are evaluated using the kinetic energy definition given in Eq. (4). The resulting variation of K^* with d for all wave conditions is presented in Fig. 15. The relationship is highly dependent on wave settings. For $T = 1.57$ s (W2), K^* exhibits a clear oscillatory trend within the investigated range, reaching values as high as 9.5, corresponding to a substantial amplification relative to the no-wall case. However, a shift of only 1 m in wall position can reduce K^* below unity, indicating a less efficient configuration than the reference case.

For the other wave periods, a similar oscillatory tendency is suggested, although the available range of d is insufficient to confirm a complete cycle. In both cases, regions of enhanced response ($K^* > 1$) and

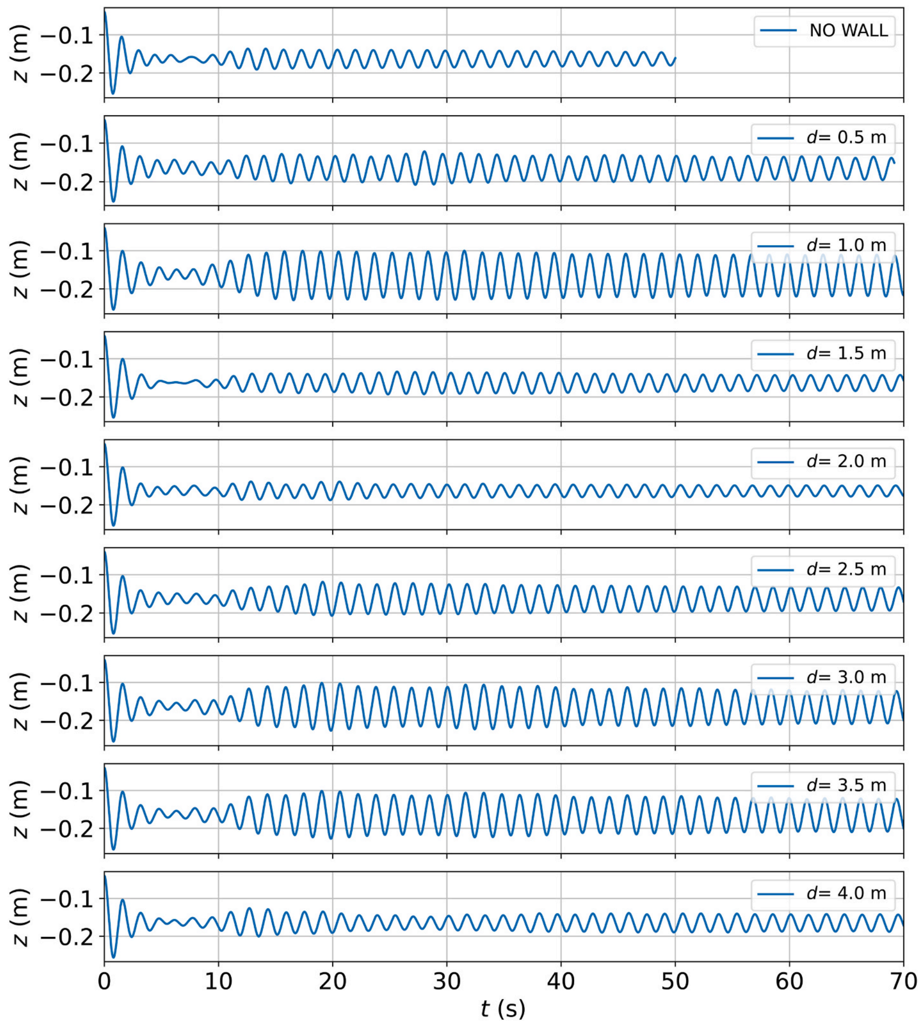

Fig. 13. Time series of the z-position of the centre of mass of the WEC at varying distances from the wall, d for the second wave setting ($T = 1.57$ s). The output of the case without a wall is also given at the top panel for comparison.

attenuation ($K^* < 1$) are observed, reinforcing the strong sensitivity of the energy capture to wall proximity.

The oscillatory variation of K^* with d can be interpreted as a result of interference between incident waves and waves reflected by the vertical wall. The superposition of these components produces a spatial modulation of the wave field in front of the wall, leading to standing-wave-like behaviour in which local hydrodynamic quantities vary periodically with distance.

Since the WEC response is primarily driven by local fluid particle velocity, spatial variations in the wave-induced velocity field directly translate into variations in the device's kinetic energy. This qualitatively suggests interference between the incoming wave and the wave fully reflected by the vertical wall. In a simplified theoretical representation, the free surface elevation, η, can be expressed as:

$$\eta(x,t) = A\cos(kx - 2\pi ft) + AR\cos(kx + 2\pi ft) \tag{5}$$

where k is the wave number and f is the wave frequency. The second term on the right-hand side represents the reflected wave with reflection coefficient R. For near-perfect reflection ($R \approx 1$), the resulting field forms a standing wave with spatial modulation proportional to:

$$\eta(x) \propto \cos(kx) \tag{6}$$

In this framework, the distance d between the WEC and the wall determines the phase of the reflected wave at the device location, i.e. kd, which governs constructive or destructive interference. Consequently, the oscillatory behaviour of K^* with d is attributed to alternating constructive and destructive interference conditions. At locations where the reflected and incident wave components are in phase, wave orbital velocities are amplified, resulting in increased WEC motion and higher kinetic energy. Conversely, out-of-phase conditions lead to partial cancellation of orbital velocities and reduced device response.

The spacing between successive peaks in the $K^*(d)$ curve for the only case exhibiting a complete oscillation within the investigated range (W2) (Fig. 15) is approximately 2.2 m, which is slightly larger than $\lambda/2 \approx 1.8$ m. This observation supports standing wave theory in front of a reflecting boundary that the oscillatory behaviour is governed primarily by the incident wavelength and the resulting wave interference pattern. The discrepancy between the measured spacing and the idealised $\lambda/2$ value suggests that local nonlinear effects and viscous interactions also influence the response.

Changing the wave period modifies the wavelength through the linear dispersion relation. As a result, the spatial interference pattern between incident and reflected waves is altered, shifting the locations of constructive and destructive interference. This explains why the minima and maxima of K^* occur at different values of d for different wave periods. Shorter waves lead to more rapid spatial oscillations with respect to d, whereas longer waves produce broader modulation patterns.

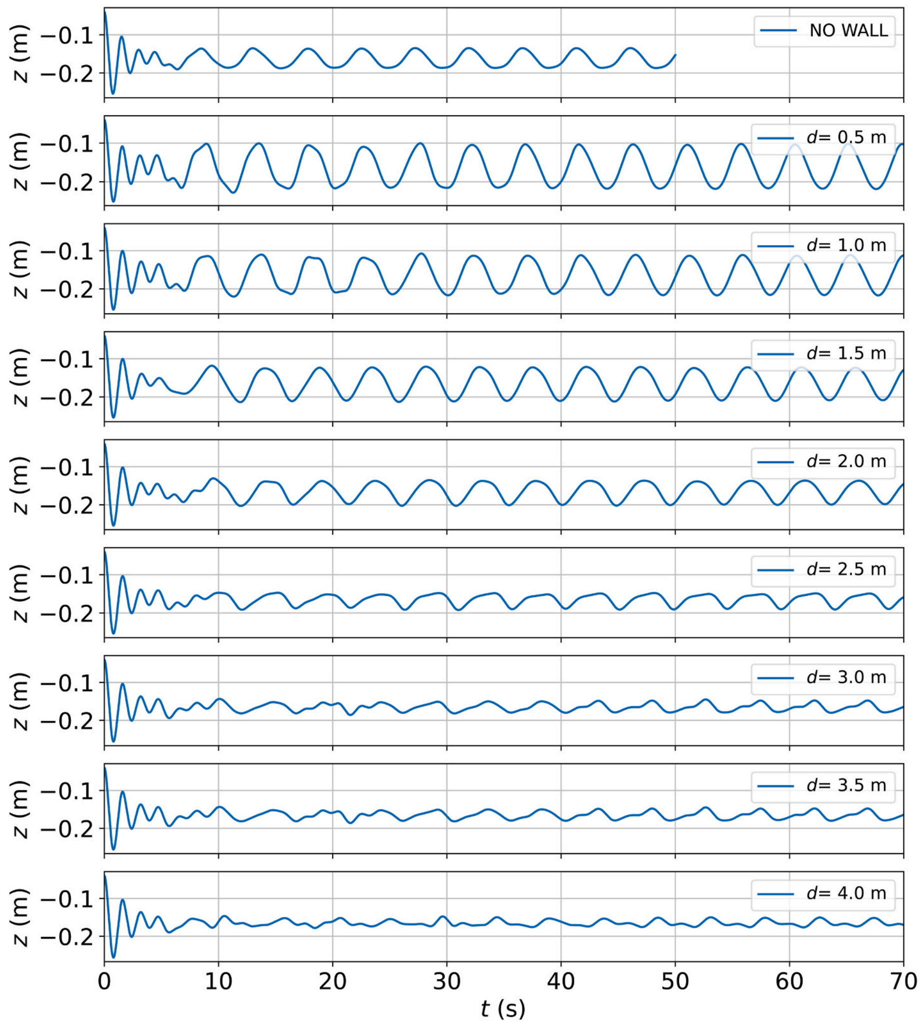

Fig. 14. Time series of the z-position of the centre of mass of the WEC at varying distances from the wall, d for the third wave setting ($T = 4.71$ s). The output of the case without a wall is also given at the top panel for comparison.

4. Conclusion

A three-dimensional CFD model was developed and applied to investigate the hydrodynamic interaction between a cylindrical buoy-type wave energy converter (WEC) and a vertical marina wall. The study demonstrated that convergence assessment based solely on global or kinematic quantities, such as the vertical displacement of the device, can be misleading. While the WEC motion exhibited apparent convergence at relatively coarse mesh resolutions, turbulence quantities required substantially finer resolution, with y^+ values on the WEC surface remaining lower than 5 at all tested simulation times, to achieve mesh-independent behaviour. This highlights that reliable CFD modelling of confined WEC environments must include turbulence-field diagnostics as part of the verification process, especially in regions dominated by strong shear, separation, and vorticity generation. Although the present study focuses primarily on device motion and kinetic energy response, unresolved turbulence structures may become particularly important when predicting hydrodynamic loads, wake dynamics, fatigue behaviour, or environmental impacts associated with near-wall deployments.

The model was then used to examine the influence of wall proximity under different wave conditions. The results show that the hydrodynamic response of the WEC is highly sensitive to the distance from the wall and varies non-monotonically due to wave reflection and interference effects. Depending on wave period and spacing, the kinetic energy response of the device exhibits strong amplification or attenuation, with variations reaching up to a factor of 9.5 relative to the no-wall case. These fluctuations are governed by the spatial structure of the reflected wave field and the resulting modulation of local orbital velocities at the device location. The results provide direct implications for device placement and optimisation within sheltered coastal infrastructures, where small positional changes can lead to large variations in energy capture.

Importantly, the study also shows that confinement effects are not solely governed by inviscid wave interference. Elevated velocity gradients near the wall–WEC gap generate intensified shear layers and vorticity, increasing viscous dissipation and altering the oscillatory response of the WEC. This indicates that both wave-phase interference and viscous–turbulent processes must be resolved to accurately predict performance in near-wall deployments.

CRediT authorship contribution statement

Burhan Yildiz: Conceptualization, Formal analysis, Investigation, Methodology, Software, Validation, Visualization, Writing – original draft. **Davide Dapelo:** Conceptualization, Supervision, Writing – review & editing. **Musa Bashir:** Conceptualization, Funding acquisition, Writing – review & editing. **Nick J. Baker:** Conceptualization, Writing – original draft, Writing – review & editing. **Rose Norman:** Conceptualization, Writing – review & editing. **Kayvan Pazouki:**

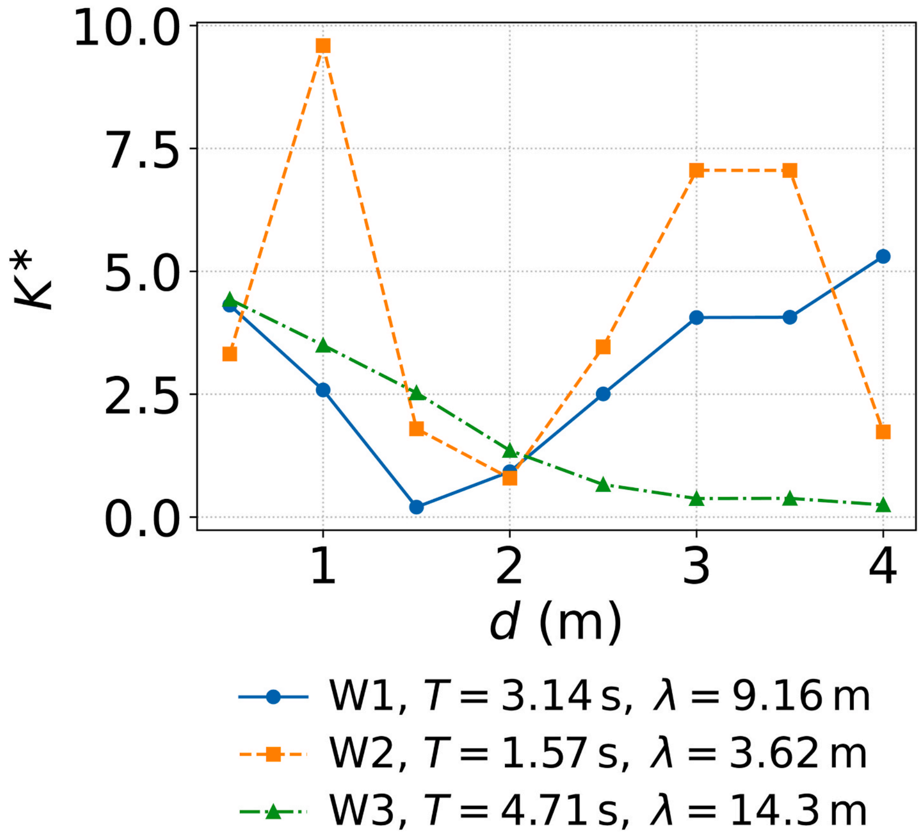

Fig. 15. Variation of normalized kinetic energy, K^*, with the distance between the WEC and wall, d.

Conceptualization, Writing – review & editing.

Declaration of competing interest

The authors declare that they have no known competing financial interests or personal relationships that could have appeared to influence the work reported in this paper.

Acknowledgments

The authors gratefully acknowledge financial support from United Kingdom Research and Innovation (UKRI) through the SMARTGEN project (grant reference 10130562), and the computational resources provided by the Barkla supercomputer at the University of Liverpool. The electrical machine research for this work was funded by Engineering and Physical Sciences Research Council grant number EP/V040758/1.

References

Alletto, M., 2022. Comparison of overset mesh with morphing mesh: flow over a forced oscillating and freely oscillating 2D cylinder. OpenFOAM J. 2, 13–30. https://doi.org/10.51560/ofj.v2.47.

Arrosyid, W.A., Sari, W.R., Waskito, K.T., Utama, I.K.A.P., Soesanto, Q.M.B., Bramantya, A., Nugroho, B., 2025. Recent advancements in wave energy converter technologies: a comprehensive review on design and performance optimization. Ocean Eng. 340, 122328. https://doi.org/10.1016/j.oceaneng.2025.122328.

Astariz, S., Iglesias, G., 2015. The economics of wave energy: a review. Renew. Sustain. Energy Rev. 45, 397–408. https://doi.org/10.1016/j.rser.2015.01.061.

Baker, N., Chambers, L., Turkmen, S., 2023. Design of an integrated generator and heaving buoy. In: Proceedings of the European Wave and Tidal Energy Conference, 15. https://doi.org/10.36688/ewtec-2023-268.

Baker, N., Turkment, S., Halibese, N., Farahani, E.F., 2025. Hydrodynamic design and build of a direct drive heaving buoy wave energy converter. In: Proceedings of the European Wave and Tidal Energy Conference, 16. https://doi.org/10.36688/ewtec-2025-771.

Bharath, A., Nader, J.R., Penesis, I., Macfarlane, G., 2018. Nonlinear hydrodynamic effects on a generic spherical wave energy converter. Renew. Energy 118, 56–70. https://doi.org/10.1016/j.renene.2017.10.078.

Chen, W., Dolguntseva, I., Savin, A., Zhang, Y., Li, W., Svensson, O., Leijon, M., 2017. Numerical modelling of a point-absorbing wave energy converter in irregular and extreme waves. Appl. Ocean Res. 63, 90–105. https://doi.org/10.1016/j.apor.2017.01.004.

Ding, H., 2024. Hydrodynamic performance of a dual-pontoon WEC-breakwater system: an analysis of wave energy content and converter efficiency. Energies 17 (16), 4046. https://doi.org/10.3390/en17164046.

Ducrozet, G., Bonnefoy, F., Le Touzé, D., Ferrant, P., 2016. HOS-ocean: open-Source solver for nonlinear waves in open ocean based on high-order spectral method. Comput. Phys. Commun. 203, 245–254. https://doi.org/10.1016/j.cpc.2016.02.017.

Farahani, E.F., Baker, N.J., Mahmouditabar, F., 2023. An innovative h-type flux switching permanent magnet linear generator for thrust force enhancement. Energies 16 (16), 5976. https://doi.org/10.3390/en16165976.

Foteinis, S., 2022. Wave energy converters in low energy seas: current state and opportunities. Renew. Sustain. Energy Rev. 162, 112448. https://doi.org/10.1016/j.rser.2022.112448.

Guo, B., Ringwood, J.V., 2021. A review of wave energy technology from a research and commercial perspective. IET Renew. Power Gener. 15 (14), 3065–3090. https://doi.org/10.1049/rpg2.12302.

Heo, S., Koo, W., Lee, O.B., 2025. Optimization analysis of a heaving point absorber wave energy converter in wave focusing conditions near a parabolic vertical wall. Ocean Eng. 331, 121342. https://doi.org/10.1016/j.oceaneng.2025.121342.

Hirt, C.W., Nichols, B.D., 1981. Volume of fluid (VOF) method for the dynamics of free boundaries. J. Comput. Phys. 39 (1), 201–225. https://doi.org/10.1016/0021-9991(81)90145-5.

Jacobsen, N.G., Fuhrman, D.R., Fredsøe, J., 2012. A wave generation toolbox for the open-source CFD library: OpenFoam®. Int. J. Numer. Methods Fluid. 70 (9), 1073–1088. https://doi.org/10.1002/fld.2726.

Jiang, L., Diao, M., Sun, H., Ren, Y., 2018. Numerical modeling of flow over a rectangular broad-crested weir with a sloped upstream face. Water 10 (11), 1663. https://doi.org/10.3390/w10111663.

Kang, Y., Zeng, X., Cui, Z., Chen, J., 2024. Hydrodynamic responses and layout optimization of wave energy converter arrays consisting of five-degree-of-freedom truncated cylinders in front of a vertical wall. Phys. Fluids 36 (1).

Kang, Y., Zeng, X., Cui, Z., Chen, J., 2025. Hydrodynamic performance and layout optimization of floating truncated cylinder wave energy converter arrays in front of a vertical wall under the action of regular and irregular waves. Phys. Fluids 37 (9). https://doi.org/10.1063/5.0288290.

Kara, F., 2021. Hydrodynamic performances of wave energy converter arrays in front of a vertical wall. Ocean Eng. 235, 109459. https://doi.org/10.1016/j.oceaneng.2021.109459.

Kara, F., 2022. Effects of a vertical wall on wave power absorption with wave energy converters arrays. Renew. Energy 196, 812–823. https://doi.org/10.1016/j.renene.2022.07.046.

Khatibani, M.J., Ghassemi, H., Ghiasi, M., 2025a. Numerical study on coupled heave-pitch motions of multi-body Salter's duck-WEC with a floating platform in regular and irregular waves. Energy Convers. Manag. X, 119639. https://doi.org/10.1016/j.enconman.2025.119639.

Khatibani, M.J., Ghassemi, H., Ghiasi, M., He, G., 2025b. Performance efficiency and energy harvesting of single and multi-duck WEC under diverse geometrical and operational scenarios. Energy Convers. Manag. X, 101024. https://doi.org/10.1016/j.ecmx.2025.101024.

Kramer, M.B., Andersen, J., Thomas, S., Bendixen, F.B., Bingham, H., Read, R., et al., 2021. Highly accurate experimental heave decay tests with a floating sphere: a public benchmark dataset for model validation of fluid–structure interaction. Energies 14 (2), 269. https://doi.org/10.3390/en14020269.

Launder, B.E., Spalding, D.B., 1974. The numerical computation of turbulent flows. Comput. Methods Appl. Mech. Eng. 3 (2), 269–289. https://doi.org/10.1016/0045-7825(74)90029-2.

Le Méhauté, B., 2013. An Introduction to Hydrodynamics and Water Waves. Springer Science & Business Media.

Li, A.J., Liu, Y., Wang, X.Y., 2024. Hydrodynamic performance of vertical cylindrical wave energy absorbers in front of a vertical wall. Phys. Fluids 36 (4).

Li, H., Shi, X., Kong, W., Kong, L., Hu, Y., Wu, X., et al., 2025. Advanced wave energy conversion technologies for sustainable and smart sea: a comprehensive review. Renew. Energy 238, 121980. https://doi.org/10.1016/j.renene.2024.121980.

Menter, F.R., 1994. Two-equation eddy-viscosity turbulence models for engineering applications. AIAA J. 32 (8), 1598–1605.

Menter, F.R., Kuntz, M., Langtry, R., 2003. Ten years of industrial experience with the SST turbulence model. Turbulence Heat Mass Transf. 4 (1), 625–632. https://api.semanticscholar.org/CorpusID:38105247.

Ning, D.Z., Shi, J., Zou, Q.P., Teng, B., 2015. Investigation of hydrodynamic performance of an OWC (oscillating water column) wave energy device using a fully nonlinear HOBEM (higher-order boundary element method). Energy 83, 177–188.

Onslow, M., Stock, A., 2025. Genetic algorithm based co-design of wave energy converter power take-off, floater geometry, and control. In: Proceedings of the European Wave and Tidal Energy Conference, 16. https://doi.org/10.36688/ewtec-2025-1013.

OpenCFD Ltd, 2026. User Guide. OpenFOAM. https://www.openfoam.com/documentation/user-guide.

Rusche, H., 2002. Computational Fluid Dynamics of Dispersed Two-phase Flow at High Phase Fractions. Ph. D. Thesis. University of London.

Satymov, R., Bogdanov, D., Dadashi, M., Lavidas, G., Breyer, C., 2024. Techno-economic assessment of global and regional wave energy resource potentials and profiles in hourly resolution. Appl. Energy 364, 123119.

Song, F., Cheng, Y., Dai, S., Yuan, Z., Incecik, A., 2024. Hydrodynamic characteristics and parametric optimizations of a hybrid system combining a hinged wave energy converter and a breakwater with a semi-opened moonpool. Energy Convers. Manag. 313, 118614. https://doi.org/10.1016/j.enconman.2024.118614.

Wang, Y., Dong, S., 2023. Theoretical investigation on integrating a heaving WEC in the semicircle opening of a vertical breakwater. J. Fluid Struct. 120, 103911.

Weller, H.G., Tabor, G., Jasak, H., Fureby, C., 1998. A tensorial approach to computational continuum mechanics using object-oriented techniques. Comput. Phys. 12 (6), 620–631. https://doi.org/10.1063/1.168744.

Wilcox, D.C., 2008. Formulation of the k-ω turbulence model revisited. AIAA J. 46 (11), 2823–2838. https://doi.org/10.2514/1.36541.

Windt, C., Davidson, J., Chandar, D.D., Faedo, N., Ringwood, J.V., 2020. Evaluation of the overset grid method for control studies of wave energy converters in OpenFOAM numerical wave tanks. J. Ocean Eng. Marine Energy 6 (1), 55–70. https://doi.org/10.1007/s40722-019-00156-5.

Windt, C., Davidson, J., Ringwood, J.V., 2018. High-fidelity numerical modelling of ocean wave energy systems: a review of computational fluid dynamics-based numerical wave tanks. Renew. Sustain. Energy Rev. 93, 610–630. https://doi.org/10.1016/j.rser.2018.05.020.

Wolgamot, H.A., Fitzgerald, C.J., 2015. Nonlinear hydrodynamic and real fluid effects on wave energy converters. Proc. Inst. Mech. Eng. A J. Power Energy 229 (7), 772–794. https://doi.org/10.1177/0957650915570351.

Yang, I., Tezdogan, T., Incecik, A., 2023. Numerical investigations of a pivoted point absorber wave energy converter integrated with breakwater using CFD. Ocean Eng. 274, 114025. https://doi.org/10.1016/j.oceaneng.2023.114025.

Yildiz, B., Uijttewaal, W.S., 2025. Estimation of discharge coefficients for free-flowing compound weirs with upstream horizontal flow contraction. J. Hydraul. Eng. 151 (4), 04025013. https://doi.org/10.1061/JHEND8.HYENG-14133.